pharmaceutics

MDPI

Article

Surface Charge-Dependent Targeting and Penetration of Magnetic Nanoparticles into Eggs and Adult Worms of *Schistosoma japonicum*

Congjin Mei [1,2,3,†], Juan Zhou [2,†], Lijun Song [3], Chuanxin Yu [3], Haihang Tang [2], Yumeng Bao [2], Yingying Yang [3], Panpan Dong [3], Yang Dai [3,*] and Jinghua Chen [2,*]

[1] School of Biotechnology, Jiangnan University, Wuxi 214122, China; meicongjin@163.com
[2] School of Life Sciences and Health Engineering, Jiangnan University, Wuxi 214122, China; juanzhou@jiangnan.edu.cn (J.Z.); 1161170133@stu.jiangnan.edu.cn (H.T.); 6233304001@stu.jiangnan.edu.cn (Y.B.)
[3] National Health Commission Key Laboratory of Parasitic Disease Control and Prevention, Jiangsu Provincial Key Laboratory on Parasite and Vector Control Technology, Jiangsu Provincial Medical Key Laboratory, Jiangsu Institute of Parasitic Diseases, Wuxi 214064, China; songlijun@jipd.com (L.S.); yuchuanxin@jipd.com (C.Y.); yangyingying@jipd.com (Y.Y.); dongpanpan@jipd.com (P.D.)
* Correspondence: daiyang@jipd.com (Y.D.); chenjinghua@jiangnan.edu.cn (J.C.)
† These authors contributed equally to this work.

Abstract

Background/Objectives: The precise elimination of *Schistosoma japonicum* eggs within host tissues poses a significant therapeutic obstacle due to the ineffectiveness of existing drugs in penetrating the eggs' protective shields. This investigation sought to create a surface-modified magnetic nanoparticle (MNP) framework to surmount this hurdle and realize targeted theranostics for combating schistosomiasis. **Methods**: Fe_3O_4 MNPs, MNP-NH_2, and MNP-COOH were synthesized and characterized before systematically studying their interactions with parasites. The intrinsic autofluorescence of eggs and adult worms served as an optical background for the investigation. In vitro co-incubation assays, confocal microscopy, and Prussian blue staining were utilized to quantify both adsorption and internalization. The in vivo efficacy was assessed in a *Schistosoma japonicum* murine model following tail vein injection. **Results**: A pronounced surface chemistry-dependent interaction was noted. Fe_3O_4 MNP and MNP-NH_2 displayed remarkable adsorption and effective internalization into eggs in vitro, while MNP-COOH exhibited limited uptake. This varying effectiveness was similarly observed in vivo, with Fe_3O_4 MNP and MNP-NH_2 predominantly gathering in hepatic granulomas and effectively infiltrating deposited eggs. Within adult worms, Fe_3O_4 MNP and MNP-COOH exhibited distribution on the tegument and within adult worms. **Conclusions**: We developed a functional MNP platform in which surface charge governs parasiticidal targeting. Among the candidates investigated, MNP-NH_2 proved to be the most efficient for egg-targeted theranostics. This study introduces an innovative nanotechnology-based approach for accurate diagnosis and treatment of schistosomiasis by specifically tackling the challenge of impermeable eggs.

Keywords: *Schistosoma japonicum*; magnetic nanoparticles; eggs; adults

Check for updates

Academic Editor: Avi Domb

Received: 15 January 2026
Revised: 9 February 2026
Accepted: 10 February 2026
Published: 11 February 2026

Copyright: © 2026 by the authors. Licensee MDPI, Basel, Switzerland. This article is an open access article distributed under the terms and conditions of the Creative Commons Attribution (CC BY) license.

1. Introduction

Schistosomiasis is a zoonotic parasitic disease that is widely prevalent in tropical and subtropical regions [1]. Globally, around 760 million people live in endemic areas, with

close to 200 million infections and approximately 200,000 deaths reported annually [2]. The high prevalence of this disease has substantially hindered social stability and economic development in affected regions. Human schistosomiasis is primarily caused by three species: *Schistosoma japonicum* (*S. japonicum*), *Schistosoma mansoni* (*S. mansoni*), and *Schistosoma haematobium* (*S. haematobium*) [3]. In China, *S. japonicum* is the endemic species, with concentration along the Yangtze River [4]. Adult schistosome worms mature and deposit their eggs within the portal vein system [5]. A significant number of these eggs migrate through the bloodstream into the smaller branches of the portal vein in the liver, leading to embolism and stimulating the surrounding tissues. This process induces a series of pathological changes and promotes the proliferation of fibrous tissue, ultimately resulting in liver fibrosis [6,7]. Accurate diagnosis and effective treatment can not only prevent the spread and prevalence of schistosomiasis, but also prevent the damage to the host in time [8,9]. At present, the prevalence of schistosomiasis is mainly characterized by low degree infection [10], and the traditional diagnostic technology is not sensitive to patients with early infection of schistosomiasis [11,12], resulting in a high rate of missed diagnosis and misdiagnosis, which has become a difficult clinical disease and directly affects the cure rate. Secondly, schistosomiasis is a parasitic disease affecting various tissues and organs. Traditional detection methods often struggle to accurately locate samples, rendering the process both challenging and distressing, which complicates the diagnosis of schistosomiasis. Consequently, direct monitoring and treatment of schistosome adult or egg infections in vivo represent a more efficient strategy for diagnosis and management.

The theranostics paradigm, integrating therapeutic and diagnostic functions into a unified platform, presents a promising approach to tackle these dual challenges. In the case of schistosomiasis, a theranostic agent could facilitate both the non-invasive imaging of egg clusters for disease severity evaluation and the precise administration of an ovicidal payload to the same sites. Magnetic nanoparticles, possessing intrinsic responsiveness to external magnetic fields and the ability for surface functionalization, emerge as a prime candidate for constructing a focused theranostic system against *S. japonicum*.

Studies have shown that eggshells of *S. japonicum* and *S. mansoni* contain iron [13,14]. The iron is believed to help stabilize the proteins that form the eggshells. The Helmintex™ method, which is based on the interaction between schistosome eggs and magnetite-coated microspheres, has proven to be sensitive for the detection of schistosome eggs [15,16]. Studies by Renata R.F. Candido et al. showed that there was an interaction between magnetic microspheres (~4 μm) and the eggs [17].

In recent years, the application of nanomaterials in the biomedical field has gained prominence due to their unique properties [18]. Fe_3O_4 magnetic nanoparticles (Fe_3O_4 MNPs) have emerged as a focal point of research, attributed to their distinctive superparamagnetism [19], excellent biocompatibility [20], and targeting capabilities [21]. When subjected to a magnetic field, Fe_3O_4 MNPs demonstrate remarkable magnetic responsiveness. Their roles in targeted drug delivery, magnetic resonance imaging (MRI), and magnetic thermal effects present a promising strategy for tumour therapy [22,23].

The surface chemical modification of functional nanoparticles plays a pivotal role in regulating their biological interface behaviour, a principle that has been extensively validated within the biomedical domain. Research has demonstrated that iron oxide nanoparticles functionalised with specific ligands can markedly enhance their cell targeting and binding efficiency, underscoring the universal significance of surface engineering in precise biomolecular recognition [24]. Notably, this principle also exhibits promising applications in parasitology-related systems. For example, in the intermediate host of schistosome, *Biomphalaria glabrata*, the biological effects and cumulative distribution of functional iron oxide nanoparticles display a distinct dependence on surface chemistry [25].

However, the direct application of this surface chemical regulation strategy to the *S. japonicum* pathogen, particularly regarding systematic investigations of the interactions between magnetic nanoparticles modified with various functional groups and adult *S. japonicum* as well as its eggs, remains unexplored. This identified knowledge gap highlights the necessity of investigating the direct interactions between surface-modified nanoparticles and parasites as a crucial and underdeveloped research avenue.

Inspired by the above work and considering the characteristics of nanoparticles, we co-cultured MNPs (~10 nm) with schistosome eggs and adult worms, observed and analyzed the situation of the former entering the eggs or adult worms, so as to provide a plan for the subsequent development of drug delivery systems for schistosome eggs or adult worms.

Hence, our objective was to create a surface-engineered magnetic nanoparticle (MNP) with the ability to actively target and penetrate *S. japonicum* eggs for theranostic purposes. We posited that the surface chemistry of MNPs plays a crucial role in determining their interaction with schistosome parasites. We proposed that strategic design modifications, such as amino functionalization, could surmount the electrostatic and physical obstacles presented by the eggshell. While magnetic particles have previously been utilized for the ex vivo isolation and diagnosis of schistosome eggs [16], our study marks a significant conceptual departure. We concentrate on systematically assessing surface chemistry-driven targeting for in vivo therapeutic interventions and creatively exploit the inherent autofluorescence of the parasite as a natural optical background for precise monitoring of these interactions. This comprehensive approach aims to establish a fundamental strategy for converting passive nanoparticles into active, target-specific theranostic agents for combating schistosomiasis.

2. Materials and Methods

2.1. Preparation and Characterization of MNPs

The specific steps for synthesizing Fe_3O_4 MNPs and MNP-COOH particles are as follows: Dissolve 8.1 g of $FeCl_3 \cdot 6H_2O$ in 142.5 mL of deionised water and transfer the solution to a three-necked flask. Stir the mixture and heat it to 70 °C. Weigh 4.4 g of $FeCl_2 \cdot 4H_2O$ and dissolve it in 10 mL of deionised water. Filter this solution and add 7.5 mL to the three-necked flask. Under vigorous stirring, rapidly introduce 18 mL of concentrated ammonia solution with a mass fraction of 25%. After 1 min, gradually incorporate 4.66 g of oleic acid and maintain rapid stirring at 70 °C for 1 h. Upon completion of the reaction, a black sol-like substance is obtained. The resulting precipitate is separated from the reaction system using an external magnetic field. Wash the precipitate twice with ethanol to eliminate excess oleic acid, followed by washing with deionised water until the pH reaches 7. Subsequently, add 160 mL of $KMnO_4$ solution at a concentration of 10 mg/mL. The solution is subjected to ultrasonic oscillation in an ultrasonic cleaner for 8 h. After magnetic separation, wash the product three times with deionised water to yield a magnetic fluid. Alternatively, following washing, perform vacuum freeze-drying for 40 h to obtain magnetic nanoparticles with carboxyl groups modified on their surface [26,27]. The procedure for directly functionalizing magnetite nanoparticles with APTES (3-Aminopropyltriethoxysilane) is outlined as follows: A mixture of 40 mL of Fe_3O_4 NPs dispersed in water (2 g/L), 40 mL of ethanol, and 1.6 mL of a 2% v/v APTES solution was maintained at a constant temperature of 50 °C for 24 h [28]. Subsequently, each sample underwent magnetic washing using ethanol followed by Milli-Q water (MilliQ Academic from Merck Millipore, Darmstadt, Germany). The Fe_3O_4 MNPs, MNP-NH_2, and MNP-COOH were dispersed in absolute alcohol and subjected to ultrasonic treatment for 20 min. The morphologies of the particles were examined using a transmission electron microscope (TEM, TalosF200X, FEI, Hillsboro, OR, USA). For TEM detection, nanoparticle suspensions

were diluted in absolute ethanol and sonicated in an ice-water bath for 20 min at a power of 60 W to ensure adequate dispersion and prevent aggregation. A 5 µL aliquot of the well-dispersed suspension was subsequently drop-cast onto a standard 300-mesh carbon-coated copper TEM grid. The grid was air-dried at room temperature before imaging. Observations were conducted using a FEI Talos F200x transmission electron microscope (Thermo Fisher Scientific, Waltham, MA, USA) operated at an acceleration voltage of 200 kV. The TEM service was provided by Hangzhou Yanqu Information Technology Co., Ltd. (Hangzhou, China). Fifty particles were randomly selected, and their size distribution was statistically analysed employing Fiji [29]. Furthermore, 1 mg of each MNP was added to 2 mL of water. Following ultrasonic treatment (6 s on, 3 s off, at 60% power and 4 °C), the resulting MNP suspensions were attracted by a neodymium-iron-boron magnet for 5 min, and the aggregation of all MNPs in response to the magnet was observed. The FTIR spectra were acquired using a Thermo Scientific™ SMART iTX™ accessory coupled to a Thermo Scientific Nicolet™ iS™50 FTIR Spectrometer. Data collection and processing were performed using the Thermo Scientific OMNIC™ software suite (version 9.2).

2.2. Establishment of Mouse Model Infected with S. japonicum

A total of twenty female C57BL/6 mice, aged 6–8 weeks, were utilised in this study. For the infection, all mice were percutaneously infected with 15 ± 1 *S. japonicum* cercariae using the abdominal patch method [30]. The infected animals were randomly assigned to four experimental groups (n = 5 per group): the WTSJ group, comprising mice infected with *S. japonicum* and treated with sterile PBS via tail vein injection; the Fe_3O_4 MNP group, consisting of mice infected with *S. japonicum* and treated with plain Fe_3O_4 magnetic nanoparticles; the MNP-NH_2 group, which included mice infected with *S. japonicum* and treated with amino-functionalised magnetic nanoparticles; and the MNP-COOH group, made up of mice infected with *S. japonicum* and treated with carboxyl-functionalised magnetic nanoparticles. Six weeks post-infection, the mice were anaesthetised with CO_2, and blood was collected via retro-orbital venous plexus puncture for subsequent serum separation and analysis. All animal experiments were conducted in compliance with the General Requirements for Laboratory Biosafety of the People's Republic of China (GB19489-2008) [31], and ethical approval has been granted by the Jiangsu Institute of Parasitic Diseases (approval JIPD-2025-011).

2.3. Tail Vein Injection of Three MNPs

A model of *S. japonicum* infection was established in forty C57BL/6 mice, following the methodology outlined in Section 2.2. At 28 days post-infection, the mice were randomly assigned to four treatment groups (n = 5 per group). Commencing on day 28, each group received tail vein injections every other day until the endpoint at 6 weeks post-infection. The treatment protocol was as follows: the WTSJ group received 200 µL of sterile phosphate-buffered saline (PBS); the Fe_3O_4 MNP group received 200 µL of a 0.5 mg/mL suspension of plain Fe_3O_4 magnetic nanoparticles; the MNP-NH_2 group received 200 µL of a 0.5 mg/mL suspension of amino-functionalised MNPs; and the MNP-COOH group received 200 µL of a 0.5 mg/mL suspension of carboxyl-functionalised MNPs. All nanoparticle suspensions were freshly prepared in PBS and sonicated prior to injection to ensure homogeneity. Animal health and behaviour were monitored daily throughout the treatment period.

2.4. Acquisition of Adult Worms and Eggs

Adult *S. japonicum* worms were retrieved using a modified portal perfusion method. Mice were anaesthetised at the conclusion of the experiment, and their abdominal and thoracic cavities were exposed. A 1 mL syringe equipped with a needle was introduced into the left ventricle of the heart. About 5 mL of 3.8% (w/v) sodium citrate solution, pre-

warmed to 37 °C, was gently administered through the left ventricle to prompt systemic heparin reversal and vasodilation. Simultaneously with the initiation of the infusion, the mesenteric vein was incised. The effluent from this vein was amassed in a Petri dish, washed with pre-warmed phosphate-buffered saline (PBS, pH 7.4), and utilized for subsequent analyses [32]. Eggs were obtained following the established protocol detailed in the relevant literature [33], with minor modifications to the described method. The specific steps for egg retrieval were as follows: Six weeks post-infection, the livers of *S. japonicum*-infected mice were harvested, minced, and subsequently placed in 60 mL of collagenase digestion solution (1 mg/mL of type IV collagenase (Sigma, St. Louis, MO, USA, 9001-12-1) prepared with 1.2% NaCl, containing 1% penicillin and streptomycin (Servicebio, Wuhan, China, G4003)). The enzymatic digestion protocol was adapted from established methods that preserve egg integrity [34,35], and the structural intactness of isolated eggs was confirmed by microscopic examination prior to use. This mixture was digested overnight at 37 °C with agitation at 160 rpm. The following day, the digested liver solution was filtered through a 120-mesh sieve, centrifuged at 800× *g* for 5 min, and the supernatant was discarded. The precipitate was washed repeatedly with 1.2% NaCl solution until only the golden-yellow *S. japonicum* eggs remained.

2.5. Detection of the Surface Charge of Eggs

Two thousand eggs were dispersed in water and evenly distributed in a measurement cell to determine their surface charge using the Malvern Nano Zetasizer Particle Size and Zeta Potential Analyzer (Zetasizer Nano ZS Zen 3600, Malvern Panalytical, Malvern, UK).

2.6. Co-Incubation of Eggs/Adult Worms with MNPs

Fifteen milligrams of Fe_3O_4 MNP, MNP-NH_2, or MNP-COOH were added to 30 mL of RPMI 1640 medium containing 0.36 g of NaCl powder to prepare a hypertonic medium with nanoparticles (the final concentration of the particles was 0.5 mg/mL, and the final concentration of NaCl was 1.2%). Following ultrasonic treatment (6 s of ultrasound, 3 s of pause, at 60% power, maintained at 4 °C), the mixture was sterilised in a clean bench and subsequently co-cultured with 2000 eggs and five pairs of adult worms at 37 °C and 160 rpm. The time intervals for egg culture were established at 0.5 h, 1.5 h, 3 h, and 6 h, while the time interval for adult worm culture was set at 3 h and 12 h. After co-incubation, the eggs were collected, filtered through a 300-mesh sieve to eliminate excess nanoparticles, washed three times with 1.2% NaCl solution, and fixed in 4% paraformaldehyde for 24 h. The binding between MNPs and the eggs was then observed using an upright microscope (OLYMPUS BX63, Tokyo, Japan).

2.7. Microscopic Observation of Adult Worms and Eggs

Adult worms and eggs were examined using an upright fluorescence microscope under various excitation wavelengths to assess their intrinsic autofluorescence. DAPI channel: excitation at 365 nm, with emission collected at 445/50 nm; FITC channel: excitation at 488 nm, with emission collected at 525/50 nm; PE (phycoerythrin) channel: excitation at 561 nm, with emission collected at 610/60 nm. Bright-field (transmitted light) and differential interference contrast (DIC) imaging were conducted concurrently, utilising no specific fluorescence filter sets to furnish complementary morphological details. The eggs, which had been co-incubated for 6 h, were selected and scanned layer by layer using a confocal laser scanning microscope (OLYMPUS FV3000, Tokyo, Japan).

2.8. Prussian Blue Staining

The embedding of the eggs should adhere to the pattern established by the organoids [36]. Solidified agarose blocks containing the eggs were sectioned into con-

tinuous slices with a thickness of 4 μm and subsequently stained in accordance with the Prussian blue staining protocol (Servicebio, Wuhan, China, GP1068) to examine the distribution of iron ions within the eggs. Tissues from the heart, liver, spleen, lung, and kidney were also embedded and sectioned for Prussian blue staining, utilising kits obtained from Wuhan Service Bio-Technology Co., Ltd. (Servicebio, Wuhan, China, GP1068).

2.9. Statistical Analysis

Data in this study are presented as means ± SEM, unless stated otherwise. All statistical analyses were performed using GraphPad Prism 9 (version 9.3.1.471), utilizing Student's t-test, one-way ANOVA, the Mann–Whitney U test, or the Kruskal–Wallis test to assess statistical significance, with a *p*-value of less than 0.05 deemed significant.

3. Results

3.1. Characterization of Three Types of MNPs

TEM micrographs indicated that the synthesised Fe_3O_4 MNP, MNP-NH_2, and MNP-COOH nanoparticles predominantly exhibited a spherical morphology (Figure 1A). TEM analysis verified that all synthesized nanoparticles (Fe_3O_4 MNP, MNP-NH_2, MNP-COOH) displayed a consistent spherical shape, averaging around 10 nm in diameter (Figure 1B). Notably, all three types of particles maintained a mean diameter approximately equal to 10 nm, with the bare Fe_3O_4, MNP-NH_2, and MNP-COOH measuring 11.40 ± 2.63 nm, 9.96 ± 1.64 nm, and 10.36 ± 1.85 nm (Figure 1B), respectively. These measurements, along with the symmetric distribution profiles, demonstrate that the functionalization process effectively preserved the core particle size within the nanoscale regime. In examining the strength of magnetism, we initially employed a magnet to attract MNPs uniformly dispersed in water. It was observed that Fe_3O_4 MNPs and MNP-NH_2 responded rapidly to the magnetic attraction, whereas only a portion of MNP-COOH was retained by the magnet (Figure 1C). Fourier-transform infrared (FTIR) spectroscopy was utilized to characterise the three types of MNPs. The spectrum of Fe_3O_4 MNPs displays a characteristic absorption peak at approximately 532 cm^{-1} (Figure 1D, Table S1), attributed to the Fe–O lattice vibrations of the Fe_3O_4 core [37,38]. For MNP-NH_2, alongside the Fe–O peak at 535 cm^{-1}, a distinct band at 1612 cm^{-1} (Figure 1D, Table S2) is assigned to the N–H bending vibrations [39], thereby confirming the successful grafting of the amine group. In the case of MNP-COOH, a notable peak appears at 1383 cm^{-1} (Figure 1D, Table S3), corresponding to the asymmetric and symmetric stretching vibrations of the carboxylate group ($–COO^-$) [39], which indicates the presence of deprotonated carboxyl groups on the surface. These findings unequivocally demonstrate the successful functionalization of the Fe_3O_4 surface with amine and carboxyl groups, respectively.

3.2. Characteristics of Eggs

Optical analysis demonstrated that the eggs displayed autofluorescence covering a wide range, emitting measurable signals under various excitation wavelengths, including blue, green, and red (Figure 2A). Additionally, assessment of surface charge through zeta potential measurements revealed that the eggs carried a slightly negative surface charge, with an average zeta potential of around −1.50 mV (Figure 2B). The concurrent presence of autofluorescence and a marginally negative surface charge confers unique physicochemical characteristics upon the eggs.

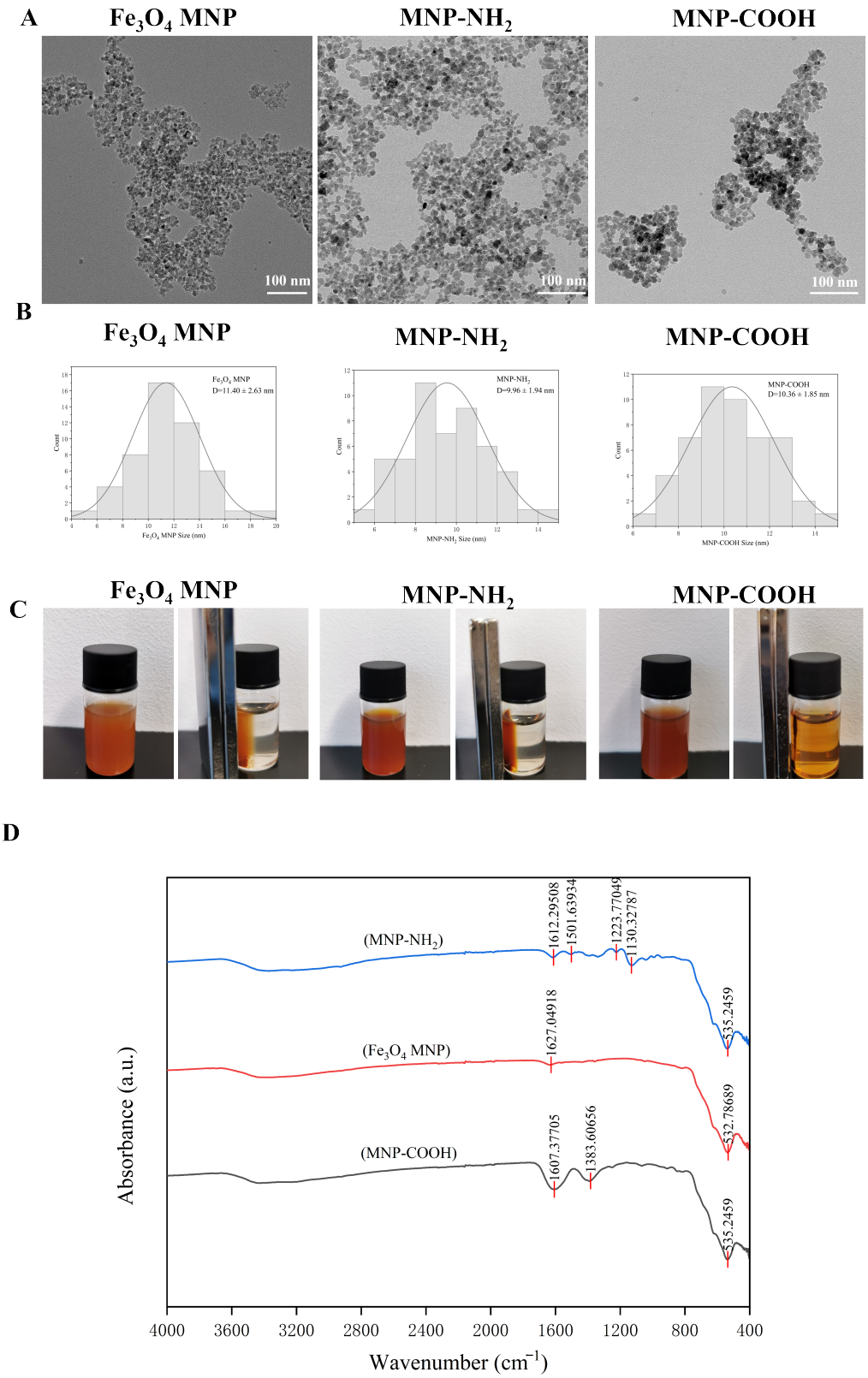


Figure 1. Characteristics of magnetic nanoparticles. (**A**) TEM images of Fe_3O_4 MNP, MNP-NH_2 and MNP-COOH; (**B**) The particle size distribution diagrams of the three MNPs; (**C**) Testing of the ability of three MNPs to respond to magnet attraction; (**D**) The infrared absorption spectra of three MNPs. scale: 100 nm.

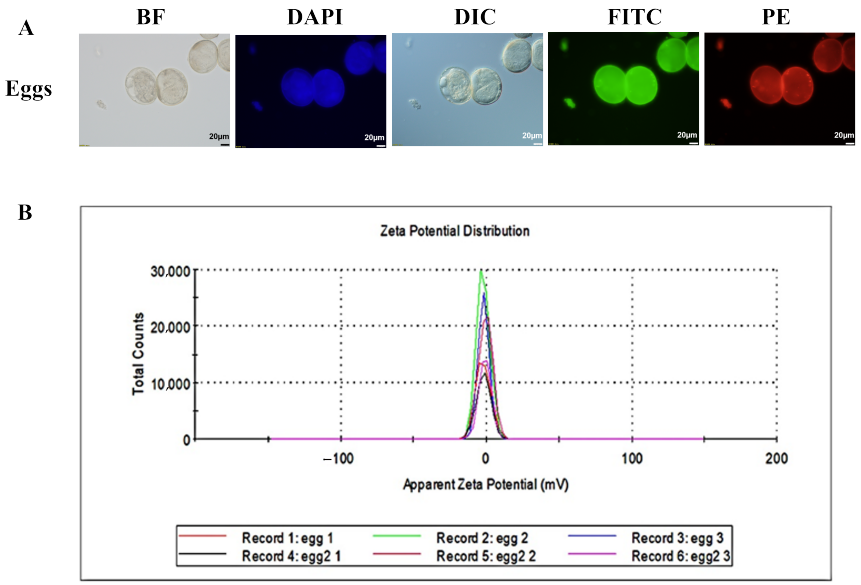


Figure 2. Characteristics of eggs. (**A**) Eggs viewed through BF and their natural autofluorescence in three distinct spectral channels. Colour-coded to match their typical emission colours: blue for the DAPI channel (365 nm excitation), green for the FITC channel (488 nm excitation), and red for the PE channel (561 nm excitation). Additionally, a differential interference contrast (DIC) image is provided for structural context. (**B**) Surface charge of eggs detected by dynamic light scattering (DLS). scale: 20 μm. DAPI (excitation 365 nm, emission 445/50 nm), FITC (excitation 488 nm, emission 525/50 nm), PE (excitation 561 nm, emission 610/60 nm), Differential Interference Contrast (DIC), and bright-field (BF).

3.3. Characteristics of Adult Worms

Broad-spectrum autofluorescence was observed in adult worms of both genders across various excitation wavelengths. In males, autofluorescence was evenly distributed throughout the body, whereas females displayed highly concentrated autofluorescence in the reproductive organs, notably in the area corresponding to the uterus (Figure 3).

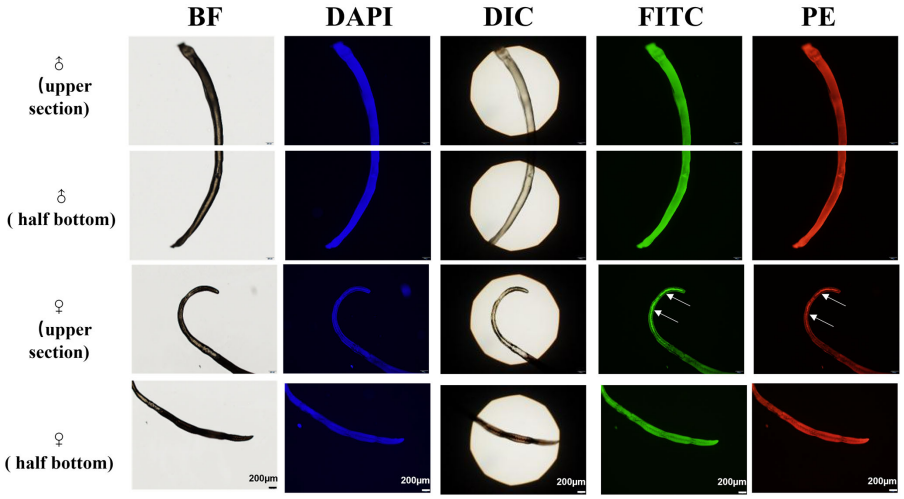


Figure 3. Adult worms viewed through BF and their natural autofluorescence in three distinct spectral channels. Colour-coded to match their typical emission colours: blue for the DAPI channel (365 nm excitation), green for the FITC channel (488 nm excitation), and red for the PE channel (561 nm excitation). Additionally, a differential interference contrast (DIC) image is provided for structural context. DAPI (excitation 365 nm, emission 445/50 nm), FITC (excitation 488 nm, emission 525/50 nm), PE (excitation 561 nm, emission 610/60 nm), Differential Interference Contrast (DIC), and bright-field (BF). The arrows indicated the spontaneous fluorescent eggs inside the adult worms.

3.4. Fe_3O_4 MNP and MNP-NH_2 Can Enter into Eggs In Vitro

Microscopic examination indicated a time-dependent rise in nanoparticle aggregation on the eggshell surface for both Fe_3O_4 MNP and MNP-NH_2 groups, as evidenced by an increasing density of dark, contrasting clusters (Figure 4A, indicated by arrows). Particularly, a noticeable yellowish-brown tint was specifically linked to the MNP-NH_2 treatment. After 6 h of co-culturing the particles with eggs, the adsorption rates were 100% for Fe_3O_4 MNP and MNP-NH_2, and 25.52% for MNP-COOH (Figure 4D). Furthermore, the colour intensity of individual eggs adsorbed by the particles displayed a progressive deepening trend with extended incubation periods, while there was no change in the NC group. Subsequently, the co-incubated eggs were subjected to 3D layer-by-layer scanning under bright field and FITC conditions. Given the intrinsic fluorescence of both eggs and adult worms (Figures 2A and 3), observation of nanoparticle entry into the eggs was conducted under FITC fluorescence excitation at a wavelength of 490 nm. The green fluorescence observed in the NC group eggs is uniformly distributed and remains unobscured by the black MNPs. In contrast, the eggs from the Fe_3O_4 MNP and MNP-NH_2 groups are obscured by these MNPs. The findings revealed superior adsorption and internalization of Fe_3O_4 MNP and MNP-NH_2 into eggs, whereas MNP-COOH particles demonstrated notably reduced efficacy (Figure 4C, Supplementary Videos S1–S4).

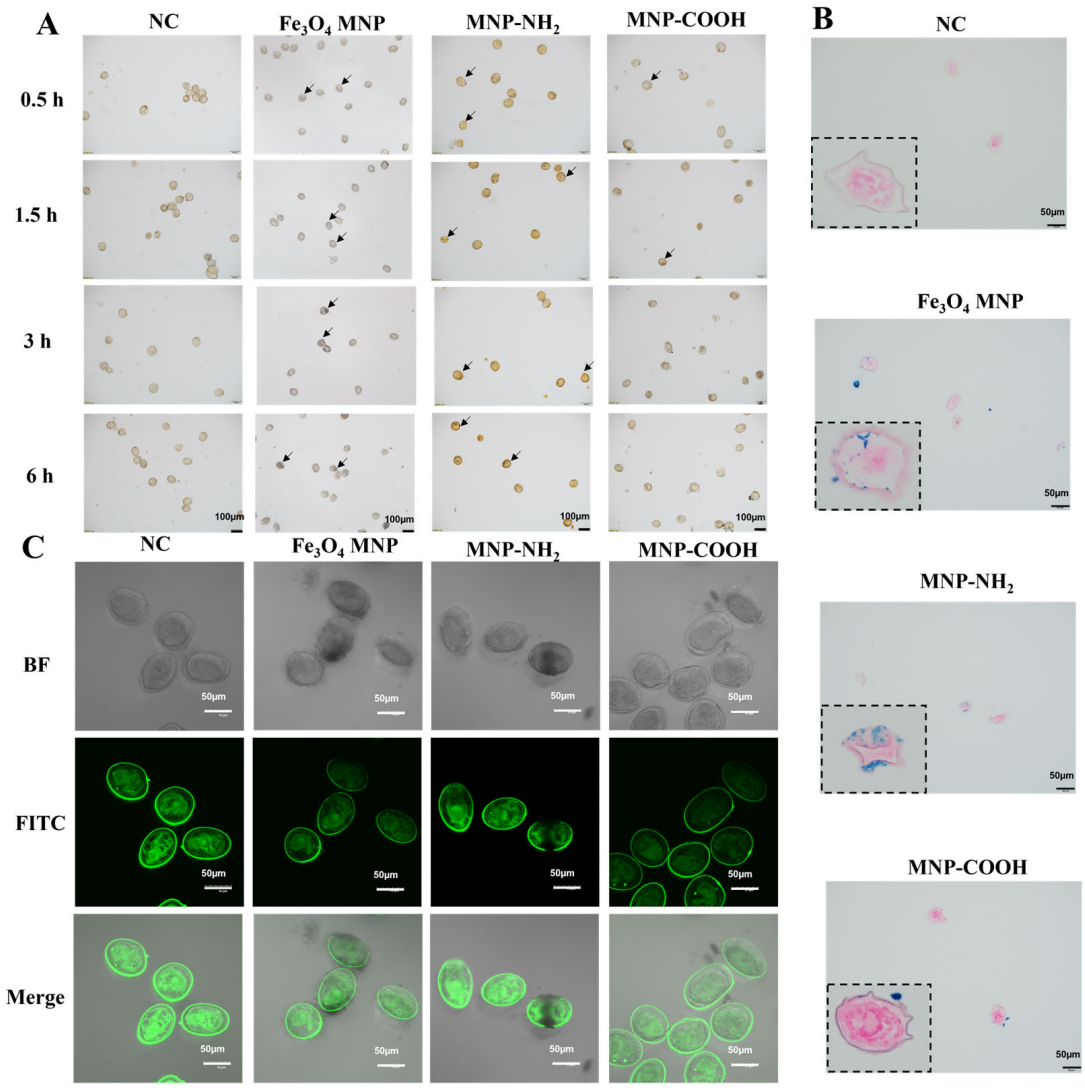


Figure 4. *Cont.*

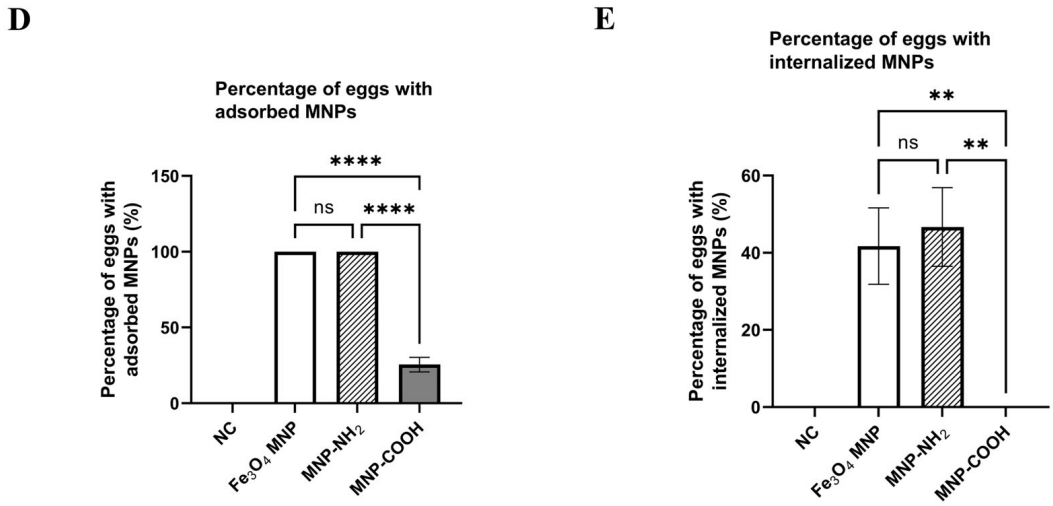


Figure 4. Interaction of Fe_3O_4 MNP, MNP-NH_2 and MNP-COOH with schistosome eggs. (**A**) Microscopic observation of the time gradient of co-incubation of three MNPs with eggs, scale: 100 μm. The arrows indicated the MNPs adsorbed around eggs (**B**) Prussian blue staining images of the interior of eggs of *S. japonicum* after 6 h of co-incubation with Fe_3O_4 MNP, MNP-NH_2 and MNP-COOH, scale: 50 μm. Blue represents iron ions (**C**) Layer-by-layer scanning of the three MNPs co-incubated with the eggs by laser confocal scanning microscope, scale: 50 μm. Green represents the spontaneous fluorescence of eggs at an excitation wavelength of 488 nm. (**D**) Percentage of eggs with adsorbed MNPs (%) after 6 h of co-incubation. (**E**) Percentage of eggs with internalized MNPs (%) after 6 h of co-incubation. FITC (excitation 488 nm, emission 525/50 nm). ** $p < 0.01$, **** $p < 0.0001$; ns, not significant.

Prussian blue staining was conducted on egg sections after a 6-h co-incubation with MNPs. The findings revealed conspicuous blue staining within schistosome eggs co-incubated with Fe_3O_4 MNP and MNP-NH_2 (Figure 4B). The internalization rates for Fe_3O_4 MNP, MNP-NH_2, and MNP-COOH were 41.74%, 46.67%, and 0%, respectively (Figure 4E), affirming the successful penetration of Fe_3O_4 MNP and MNP-NH_2 into the egg interiors. Conversely, in the group co-incubated with MNP-COOH, sporadic blue staining within the eggs suggested minimal nanoparticle infiltration, aligning with microscopic observations.

3.5. MNPs Can Enter into Eggs In Vivo

Subsequent animal experiments were conducted to confirm the presence of MNPs inside schistosome eggs in the infected liver. Prussian blue staining results revealed no discernible blue hue in the heart, lung, and kidney of mice in both control and experimental groups (Figure 5). In contrast to the WTSJ group, noticeable blue staining was observed in the Fe_3O_4 MNP and MNP-NH_2 groups in liver tissue, while it was notably fainter in the MNP-COOH group (Figure 5). These in vivo findings further evidenced a significantly higher penetration and accumulation of nanoparticles within eggs in the Fe_3O_4 MNP and MNP-NH_2 groups compared to the MNP-COOH group in liver tissue.

3.6. MNPs Can Be Ingested by Adult Worms

The eggs are produced by adult worms [40,41]. Consequently, to eliminate the eggs, it is imperative to first eradicate the adult worms at the source. We conducted experiments to investigate whether schistosome adult worms can absorb MNPs. Following co-incubation, Fe_3O_4 MNPs, MNP-NH_2, and MNP-COOH were found to be localized within both the digestive tract and the tegument of the schistosomes (Figure 6). Time-course analysis revealed distinct distribution patterns of MNPs in female adult worms. At approximately 3 h of incubation, all three types of MNPs (Fe_3O_4, MNP-COOH, and MNP-NH_2) predomi-

nantly accumulated on the surface of the integument (Figure 6A). By 12 h, a divergence in behaviour was noted: both Fe_3O_4 and MNP-COOH particles were localized within the body of adult worms, whereas MNP-NH_2 particles exhibited no evidence of internal accumulation at this time point (Figure 6B).

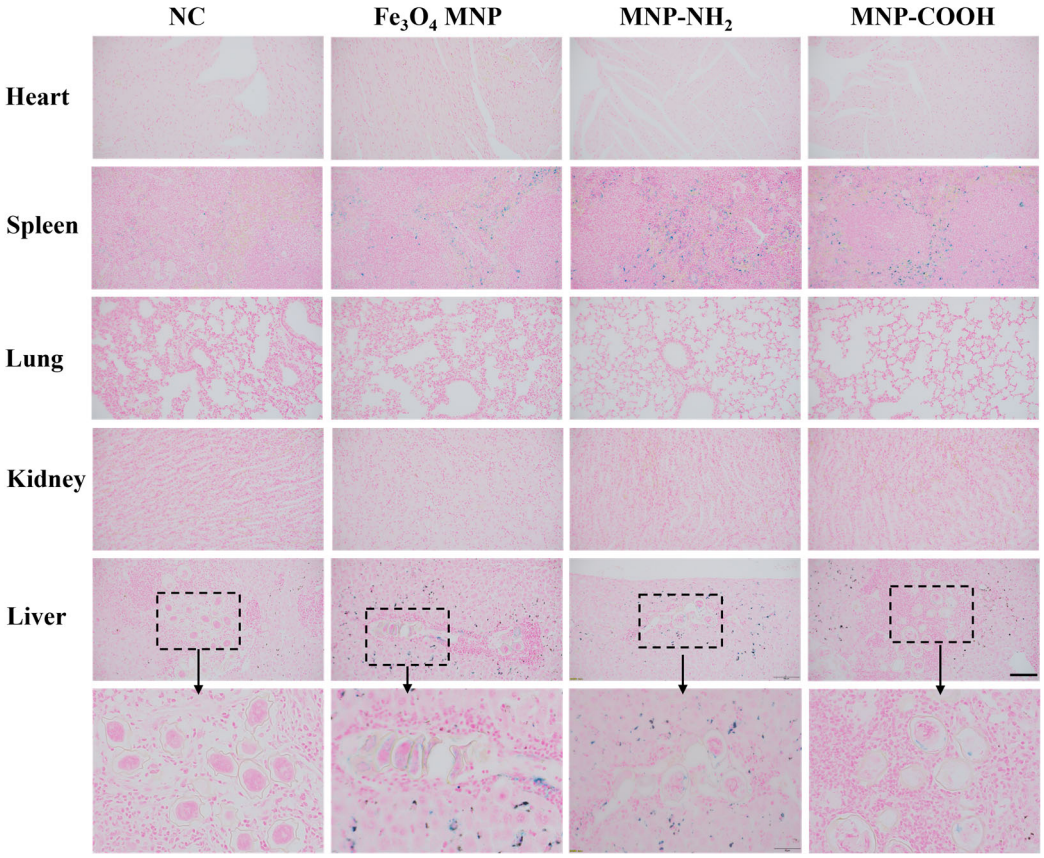


Figure 5. Prussian blue staining images of the heart, spleen, liver, lung and kidney of mice after 28 days of being infected with *S. japonicum* and then injected with MNPs. Heart: Myocardial tissue shows no specific Prussian blue-positive staining; Liver: Intense focal staining is evident within granulomatous lesions (Black dashed box); Spleen: No focal aggregates comparable to those in the liver are observed; Lung: The alveolar architecture appears normal with no detectable specific Prussian blue signals; Kidney: Renal cortex and medulla show no specific iron staining; Scale: 50 μm.

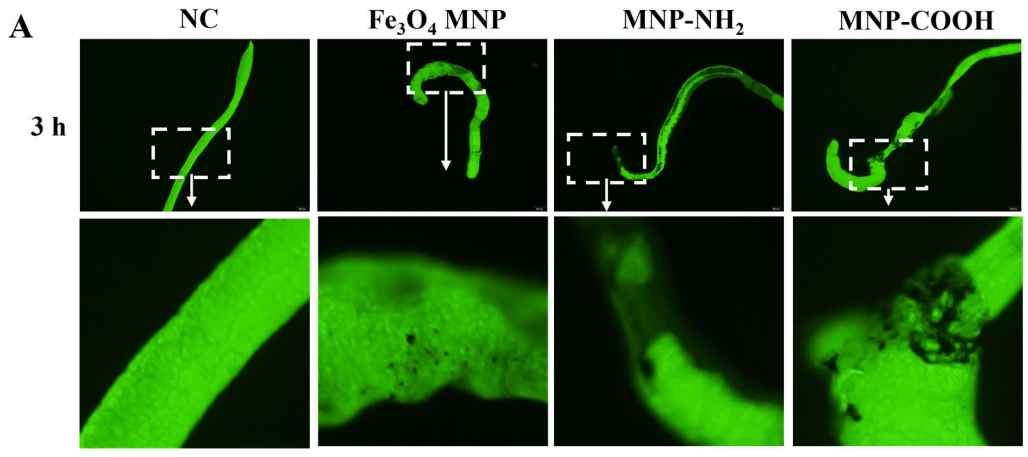


Figure 6. *Cont.*

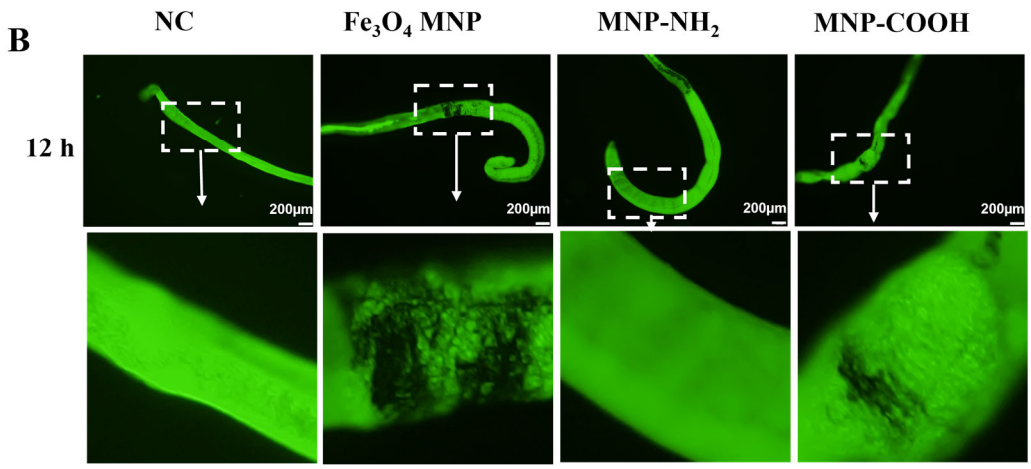


Figure 6. The co-incubation of Fe_3O_4 MNP, MNP-NH_2 and MNP-COOH with adult worms of *S. japonicum* for 3 h (**A**) and 6 h (**B**). FITC (excitation 488 nm, emission 525/50 nm). The white dashed box and arrow indicate the enlarged display of this area.

4. Discussion

During *S. japonicum* infection, the granulomatous pathology resulting from egg deposition in the liver is the main contributor to tissue damage and disease morbidity, with the eggs serving as the primary cause of injury [42]. The in vivo eradication of schistosome eggs encounters several biological challenges. The principal obstacle is the robust shell of the egg, which is composed of cross-linked proteins [43] and acts as a formidable diffusion barrier to drug molecules. Upon tissue deposition, the eggs elicit a pronounced host granulomatous inflammatory response, resulting in their tight encapsulation by fibrotic tissue [44,45]. Simultaneously, the granulomatous microenvironment is utilized by the eggs to create a localized immunoprotective niche, which allows them to evade immune clearance. As a result, even drugs that are highly effective against adult worms, such as praziquantel, prove largely ineffective against eggs [46]. Collectively, these factors represent the primary reasons why current pharmacological therapies face challenges in achieving in vivo ovicidal effects.

The results demonstrate that surface chemistry significantly influences the interaction between magnetic nanoparticles and schistosome eggs. Amino-functionalized MNPs exhibited enhanced adsorption to the egg surface and greater penetration into eggs in vitro compared with carboxyl-modified particles. In vivo, these amino-modified nanoparticles also showed a stronger tendency to accumulate at egg deposition sites in infected mice. This differential behavior indicates that nanoparticle surface charge and functional groups play a critical role in overcoming physicochemical barriers associated with the eggshell and surrounding fibrotic tissues. Collectively, these findings provide experimental evidence supporting the feasibility of surface-engineered magnetic nanoparticles for targeted localization toward schistosome eggs and highlight their potential utility in theranostic applications integrating imaging and localized delivery strategies.

The co-incubation experiments demonstrated a time-dependent increase in nanoparticle adsorption around the eggs, with a progressive enhancement of the colourimetric signal specifically noted in eggs treated with Fe_3O_4 MNP and MNP-NH_2. This variation can likely be ascribed to the functionalization of the particle surfaces. The surface modification of MNPs is crucial in determining their interaction with biological barriers [47]. Our comparative studies of functionalized particles revealed a notable disparity in both affinity and internalization efficiency among the three MNPs. MNP-NH_2 demonstrated significantly greater adsorption with eggs, while MNP-COOH particles exhibited markedly weaker attraction. This variation can be directly ascribed to the electrostatic interactions between

the nanoparticle surface and the eggshell. Building on our previous discovery of the egg surface exhibiting a slightly negative zeta potential, the positively charged MNP-NH_2 are significantly drawn towards it due to strong electrostatic forces, encouraging intimate interaction and potentially enhancing active or passive absorption. Conversely, the negatively charged MNP-COOH face electrostatic repulsion from the comparably negative egg surface, impeding attachment and subsequent incorporation. This outcome validates the significance of surface charge compatibility for precise delivery and establishes a distinct design guideline: a cationic or charge-neutral surface is most effective in improving interactions between nanoparticles and eggs. Through deliberate selection of the surface ligand, we can accurately adjust the adhesion and penetration, consequently influencing the therapeutic or diagnostic effectiveness, thus propelling the progress of highly targeted nano-theranostic systems.

Fluorescent labelling is traditionally used to trace and confirm the cellular internalization of drugs or molecules [48]. Initially, we sought to apply this established technique to determine whether nanoparticles could penetrate schistosome eggs. However, subsequent observations identified a significant confounding factor: the eggs possess intrinsic autofluorescence across multiple wavelengths. Drawing upon this inherent characteristic, we devised an alternative detection strategy that employed the eggs' autofluorescence as a built-in optical background. By utilizing the fluorescence-opaque properties of magnetic nanomaterials, we employed confocal laser scanning microscopy in conjunction with Prussian blue staining of sectioned eggs. This integrated approach conclusively demonstrated that both Fe_3O_4 MNP and MNP-NH_2 particles were effectively internalized within the eggs, while MNP-COOH particles exhibited minimal entry. This methodological adaptation not only provided direct visual evidence of nanoparticle penetration but also circumvented the limitations associated with traditional fluorescent labelling in this particular biological context. Following systemic administration through tail vein injection, Prussian blue staining of major organs, including the heart, liver, spleen, lungs, and kidneys, yielded essential in vivo validation. The results indicated a targeted accumulation of nanoparticles, predominantly within inflammatory foci in the liver, which serves as the primary site for egg deposition and pathology in schistosomiasis. This analysis notably verified the ability of nanoparticles to access ectopic egg granulomas and infiltrate eggs in vivo. In line with our in vitro results, a distinct variation in effectiveness was noted: Fe_3O_4 MNP and MNP-NH_2 demonstrated enhanced penetration into eggs within the host tissue in comparison to MNP-COOH. Various factors could account for the effective internalization of Fe_3O_4 MNP and MNP-NH_2 particles. Initially, electrostatic interactions are likely to play a critical role. The negatively charged surface of the eggs promotes the strong adsorption of positively charged or neutrally charged particles, such as Fe_3O_4 MNP and MNP-NH_2. This electrostatic attraction guarantees a high concentration of nanoparticles surrounding the egg, which is essential for subsequent internalization. In addition to surface charge, the distinctive composition and structure of the eggshell are also pivotal. It has been reported that schistosome eggshells contain paramagnetic substances [14], which may create a local attractive force on magnetic nanoparticles, thereby enhancing their accumulation around the eggs. Notably, the eggshell is not a solid barrier; rather, it is perforated by microtubules with diameters ranging from approximately 50 to 200 nm [49]. We propose that these microtubules function as direct physical channels. Nanoparticles of suitable size, such as our approximately 10 nm MNPs, can penetrate the interior of the egg via these channels. The structural hypothesis is strongly supported by our finding that magnetic microspheres of larger size (4 μm) only attach to the egg's surface without penetrating it [17], as they exceed the effective diameter of the suggested channels. In essence, the internalization

mechanism seems to be a combined outcome of electrostatic affinity, paramagnetic buildup, and ultimately, size-specific penetration through inherent shell micropores.

From a nanomaterial perspective, particle transport across biological barriers is governed by size, surface chemistry, and charge, which modulate steric obstruction, electrostatic binding, and diffusion behavior [50]. Charged biopolymers within barrier matrices can immobilize nanoparticles via electrostatic or hydrophobic interactions, while modification of surface physicochemical properties can alter retention and penetration [51]. Reviews on nanoparticle–barrier interfaces emphasize that engineered surface functionality is a major determinant of localization, internalization, and tissue distribution across diverse biological systems [52]. Therefore, the differential association observed between functionalized MNPs and schistosome eggs or worms is consistent with general principles of nano–bio interface interactions, where surface functional groups mediate adsorption to biochemical barrier components rather than passive diffusion alone. While the present observations provide phenomenological evidence of localization, detailed mechanistic elucidation will require targeted biochemical and high-resolution imaging approaches in future studies.

The eggs are produced by adult worms [40]. Expanding on the egg studies, we further examined the interaction between magnetic nanoparticles and adult worms. By utilizing the intrinsic autofluorescence of the worms alongside the fluorescence-opaque characteristics of the particles, our findings revealed that both Fe_3O_4 MNP and MNP-COOH were localised on the tegument surface and within the internal tissues of the adults. In adults, MNP uptake dynamics occur through two pathways: ingestion via the digestive tract and penetration through the integument. The presence of MNPs in the digestive system confirms oral uptake. Additionally, the detection of Fe_3O_4 MNPs and MNP-COOH within the integument directly indicates passive adsorption or active translocation. This dual-route mechanism notably increases particle concentration in adults.

The interaction between functionalized magnetic nanoparticles (MNPs) and schistosome structures can be interpreted in the broader context of nanoparticle transport across biological barriers. Adult schistosomes are enveloped by a dynamic syncytial tegument composed of proteins, lipids and carbohydrates that forms the primary host–parasite interface and mediates nutrient uptake and immune evasion. Proteomic and lipidomic studies further demonstrate that this double-membrane surface is enriched in parasite-specific lipids and proteins, indicating a complex biochemical landscape capable of selective molecular interaction [53]. The tegumental membrane contains multilaminate vesicles rich in phospholipids and discoid granules containing mucopolysaccharides, which contribute to the extracellular matrix-like ground substance at the parasite surface [54]. Such biochemical heterogeneity likely influences nanoparticle adhesion and penetration through electrostatic and hydrophobic interactions, analogous to nanoparticle behavior at mucosal or epithelial barriers.

It is important to acknowledge that the imaging-based analysis method employed in this study possesses certain inherent limitations. Firstly, while the autofluorescence quenching effect and Z-stack scanning utilized by confocal imaging facilitate semi-quantitative scoring of nanoparticle internalization (for instance, the percentage of positive eggs), they do not yield quantitative data regarding the absolute number of nanoparticles within a single egg. Secondly, the variability in autofluorescence intensity between the insect body and the egg complicates the use of these measurements as a reliable internal reference for fluorescence intensity assessment. Consequently, the associated localization analysis is predominantly qualitative or semi-quantitative in nature. Furthermore, the evaluation of the adsorption rate and specific color changes (such as the yellowish-brown hue produced by MNP-NH_2) relies entirely on manual interpretation, categorizing these observations as semi-quantitative or qualitative. Future research should implement standardized fluores-

cence labelling, quantitative elemental analysis (such as ICP-MS), and more sophisticated image analysis algorithms to acquire more precise quantitative information, thereby elucidating the dose-dependent relationship and kinetic processes governing the interaction between nanoparticles and parasites.

Our research has developed a groundbreaking framework to address parasitic infections, notably schistosomiasis. We have shown that Fe_3O_4 MNP and MNP-NH_2 can breach the eggshell barrier, enabling them to penetrate previously unreachable eggs, a pivotal progress for in vivo egg-killing treatments. Moreover, the eggs' natural fluorescence, coupled with the penetrating properties of MNPs, establishes a novel avenue for non-invasive diagnosis using contrast-based imaging. In conjunction with the identification of dual uptake pathways in adult worms, this study transitions from a passive in vitro detection model employing magnetic microspheres to an active, targeted intervention using MNPs. By integrating permeability, intrinsic biomarkers, and magnetic guidance, our research establishes a robust foundation for the next generation of therapeutic diagnostic strategies, which aim to enhance both diagnostic accuracy and therapeutic efficacy for the parasitic stages.

5. Conclusions

This study illustrates the enhanced efficacy of amino-functionalized magnetic nanoparticles (MNP-NH_2) in targeting and penetrating Schistosoma japonicum eggs, both in vitro and in a murine infection model, compared to their carboxylated (MNP-COOH) or plain Fe_3O_4 counterparts. This discovery establishes a distinct structure-activity relationship, emphasising surface charge as a critical design parameter for nano-parasite interactions. It offers empirical support for a targeted theranostic approach that leverages biological characteristics—such as the egg's negative surface charge and porous microstructure—to surmount a significant therapeutic obstacle. Consequently, this research delivers fundamental proof-of-concept for systematically designing nanocarriers to achieve precise targeting against helminthic parasites, laying the groundwork for advanced interventions integrating diagnosis and treatment.

Supplementary Materials: The following supporting information can be downloaded at: https://www.mdpi.com/article/10.3390/pharmaceutics18020231/s1, Table S1: Raw data of infrared spectra of Fe_3O_4 particles; Table S2: Raw data of infrared spectra of MNP-NH_2 particles; Table S3: Raw data of infrared spectra of MNP-COOH particles; Video S1: Layer-by-layer scanning of normal eggs by laser confocal microscopy; Video S2: Layer-by-layer scanning of eggs incubated with Fe_3O_4 MNP for 6 h by laser confocal microscopy; Video S3: Layer-by-layer scanning of eggs incubated with MNP-NH_2 for 6 h by laser confocal microscopy; Video S4: Layer-by-layer scanning of eggs incubated with MNP-COOH for 6 h by laser confocal microscopy.

Author Contributions: Conceptualization, C.M. and. J.Z.; methodology, C.M. and. J.Z.; software, H.T. and Y.B.; validation, C.M., L.S., Y.Y. and P.D.; formal analysis, L.S., Y.Y., P.D. and C.Y.; investigation, L.S., Y.Y., P.D. and C.Y.; resources, J.C.; data curation, J.Z.; writing—original draft preparation, C.M. and J.Z.; writing—review and editing, Y.D. and J.C.; visualization, C.M.; supervision, J.C. and J.Z.; project administration, J.C.; funding acquisition, Y.D. All authors have read and agreed to the published version of the manuscript.

Funding: This work was supported by the Natural Science Foundation of Jiangsu Province (BK20221538), Jiangsu Preventive Medicine Association (No. Ym2023054), "Taihu Light" Science and Technology Research Project (Basic Research, No. K20252014) and Jiangsu Province Capability Improvement Project through Science, Technology, and Education (No. ZDXYS202207).

Institutional Review Board Statement: This study adhered to the Guidelines for the Care and Use of Laboratory Animals issued by the Ministry of Science and Technology of China (No. 398, 2006).

All the experimental procedures were conducted in compliance with the General Requirements for Laboratory Biosafety in China (GB19489-2008), and the ethical approval of Jiangsu Institute of Parasitic Diseases has been obtained (approval number: JIPD-2025-011, date of approval 15 October 2025).

Informed Consent Statement: Not applicable.

Data Availability Statement: The original contributions presented in this study are included in the article/Supplementary Materials. Further inquiries can be directed to the corresponding authors.

Acknowledgments: The authors gratefully acknowledge Yang Yang for assisting with the infrared detection of MNP particles. The authors extend their gratitude to Luo Huan (from Scientific Compass) for providing invaluable assistance with the TEM analysis.

Conflicts of Interest: The authors declare no conflicts of interest.

Abbreviations

The following abbreviations are used in this manuscript:

PBS	phosphate-buffered saline
FTIR	Fourier-transform infrared
MNP	magnetic nanoparticle
S. japonicum	*Schistosoma japonicum*
S. mansoni	*Schistosoma mansoni*
S. haematobium	*Schistosoma haematobium*
MRI	magnetic resonance imaging

References

1. Yuan, Y.; Zhao, J.; Chen, M.; Liang, H.; Long, X.; Zhang, B.; Chen, X.; Chen, Q. Understanding the Pathophysiology of Exosomes in Schistosomiasis: A New Direction for Disease Control and Prevention. *Front. Immunol.* **2021**, *12*, 634138. [CrossRef] [PubMed]
2. Gryseels, B.; Polman, K.; Clerinx, J.; Kestens, L. Human schistosomiasis. *Lancet* **2006**, *368*, 1106–1118. [CrossRef]
3. Qiu, S.; Fan, X.; Yang, Y.; Dong, P.; Zhou, W.; Xu, Y.; Zhou, Y.; Guo, F.; Zheng, Y.; Yang, J.Q. *Schistosoma japonicum* infection downregulates house dust mite-induced allergic airway inflammation in mice. *PLoS ONE* **2017**, *12*, e0179565. [CrossRef]
4. Aula, O.P.; McManus, D.P.; Jones, M.K.; Gordon, C.A. Schistosomiasis with a Focus on Africa. *Trop. Med. Infect. Dis.* **2021**, *6*, 109. [CrossRef]
5. Barsoum, R.S.; Esmat, G.; El-Baz, T. Human schistosomiasis: Clinical perspective: Review. *J. Adv. Res.* **2013**, *4*, 433–444. [CrossRef]
6. McManus, D.P.; Bergquist, R.; Cai, P.; Ranasinghe, S.; Tebeje, B.M.; You, H. Schistosomiasis-from immunopathology to vaccines. *Semin. Immunopathol.* **2020**, *42*, 355–371. [CrossRef]
7. Gobbi, F.; Tamarozzi, F.; Buonfrate, D.; van Lieshout, L.; Bisoffi, Z.; Bottieau, E.; on behalf of TropNet Schisto Task Force. New Insights on Acute and Chronic Schistosomiasis: Do We Need a Redefinition? *Trends Parasitol.* **2020**, *36*, 660–667. [CrossRef]
8. Vaillant, M.T.; Philippy, F.; Neven, A.; Barre, J.; Bulaev, D.; Olliaro, P.L.; Utzinger, J.; Keiser, J.; Garba, A.T. Diagnostic tests for human *Schistosoma mansoni* and *Schistosoma haematobium* infection: A systematic review and meta-analysis. *Lancet Microbe* **2024**, *5*, e366–e378. [CrossRef] [PubMed]
9. Li, X.; Dang, Z.; Tang, W.; Zhang, H.; Shao, J.; Jiang, R.; Zhang, X.; Huang, F. Detection of Parasites in the Field: The Ever-Innovating CRISPR/Cas12a. *Biosensors* **2024**, *14*, 145. [CrossRef] [PubMed]
10. Gao, H.; Xiao, D.; Song, L.; Zhang, W.; Shen, S.; Yin, X.; Wang, J.; Ke, X.; Yu, C.; Zhang, J. Assessment of the diagnostic efficacy of enolase as an indication of active infection of *Schistosoma japonicum*. *Parasitol. Res.* **2016**, *115*, 151–164. [CrossRef]
11. Worrell, C.; Xiao, N.; Vidal, J.E.; Chen, L.; Zhong, B.; Remais, J. Field detection of *Schistosoma japonicum* cercariae in environmental water samples by quantitative PCR. *Appl. Environ. Microbiol.* **2011**, *77*, 2192–2195. [CrossRef]
12. Doenhoff, M.J.; Chiodini, P.L.; Hamilton, J.V. Specific and sensitive diagnosis of schistosome infection: Can it be done with antibodies? *Trends Parasitol.* **2004**, *20*, 35–39. [CrossRef]
13. Jones, M.K.; McManus, D.P.; Sivadorai, P.; Glanfield, A.; Moertel, L.; Belli, S.I.; Gobert, G.N. Tracking the fate of iron in early development of human blood flukes. *Int. J. Biochem. Cell Biol.* **2007**, *39*, 1646–1658. [CrossRef] [PubMed]
14. Karl, S.; Gutierrez, L.; Lucyk-Maurer, R.; Kerr, R.; Candido, R.R.; Toh, S.Q.; Saunders, M.; Shaw, J.A.; Suvorova, A.; Hofmann, A.; et al. The iron distribution and magnetic properties of schistosome eggshells: Implications for improved diagnostics. *PLoS Negl. Trop. Dis.* **2013**, *7*, e2219. [CrossRef]
15. Fagundes Teixeira, C.; Neuhauss, E.; Ben, R.; Romanzini, J.; Graeff-Teixeira, C. Detection of *Schistosoma mansoni* eggs in feces through their interaction with paramagnetic beads in a magnetic field. *PLoS Negl. Trop. Dis.* **2007**, *1*, e73. [CrossRef]

16. Favero, V.; Frasca Candido, R.R.; De Marco Verissimo, C.; Jones, M.K.; St. Pierre, T.G.; Lindholz, C.G.; Da Silva, V.D.; Morassutti, A.L.; Graeff-Teixeira, C. Optimization of the Helmintex method for schistosomiasis diagnosis. *Exp. Parasitol.* **2017**, *177*, 28–34. [CrossRef]
17. Candido, R.R.; Favero, V.; Duke, M.; Karl, S.; Gutierrez, L.; Woodward, R.C.; Graeff-Teixeira, C.; Jones, M.K.; St. Pierre, T.G. The affinity of magnetic microspheres for Schistosoma eggs. *Int. J. Parasitol.* **2015**, *45*, 43–50. [CrossRef]
18. Karki, S.; Gohain, M.B.; Yadav, D.; Ingole, P.G. Nanocomposite and bio-nanocomposite polymeric materials/membranes development in energy and medical sector: A review. *Int. J. Biol. Macromol.* **2021**, *193*, 2121–2139. [CrossRef]
19. Jiang, Y.; Kang, Y.; Liu, J.; Yin, S.; Huang, Z.; Shao, L. Nanomaterials alleviating redox stress in neurological diseases: Mechanisms and applications. *J. Nanobiotechnol.* **2022**, *20*, 265. [CrossRef] [PubMed]
20. Luo, M.; Lee, L.K.C.; Peng, B.; Choi, C.H.J.; Tong, W.Y.; Voelcker, N.H. Delivering the Promise of Gene Therapy with Nanomedicines in Treating Central Nervous System Diseases. *Adv. Sci.* **2022**, *9*, e2201740. [CrossRef] [PubMed]
21. Dash, S.; Das, T.; Patel, P.; Panda, P.K.; Suar, M.; Verma, S.K. Emerging trends in the nanomedicine applications of functionalized magnetic nanoparticles as novel therapies for acute and chronic diseases. *J. Nanobiotechnol.* **2022**, *20*, 393. [CrossRef]
22. Alev, M.; Egenberger, L.; Muhleisen, L.; Weigel, B.; Frey, B.; Friedrich, R.P.; Pottler, M.; Alexiou, C.; Janko, C. Targeting of drug-loaded nanoparticles to tumor sites increases cell death and release of danger signals. *J. Control Release* **2018**, *285*, 67–80. [CrossRef] [PubMed]
23. Li, H.; Yang, S.; Hui, D.; Hong, R. Progress in magnetic Fe_3O_4 nanomaterials in magnetic resonance imaging. *Nanotechnol. Rev.* **2020**, *9*, 1265–1283. [CrossRef]
24. Fu, Y.; Li, X.; Chen, H.; Wang, Z.; Yang, W.; Zhang, H. CXC Chemokine Receptor 4 Antagonist Functionalized Renal Clearable Manganese-Doped Iron Oxide Nanoparticles for Active-Tumor-Targeting Magnetic Resonance Imaging-Guided Bio-Photothermal Therapy. *ACS Appl. Bio Mater.* **2019**, *2*, 3613–3621. [CrossRef]
25. Pena, R.V.; Machado, R.C.; Caixeta, M.B.; Araujo, P.S.; de Oliveira, E.C.; da Silva, S.M.; Rocha, T.L. Lauric acid bilayer-functionalized iron oxide nanoparticles disrupt early development of freshwater snail *Biomphalaria glabrata* (Say, 1818). *Acta Trop.* **2022**, *229*, 106362. [CrossRef]
26. Zhang, S.; Zhao, X.; Niu, H.; Shi, Y.; Cai, Y.; Jiang, G. Superparamagnetic Fe_3O_4 nanoparticles as catalysts for the catalytic oxidation of phenolic and aniline compounds. *J. Hazard. Mater.* **2009**, *167*, 560–566. [CrossRef] [PubMed]
27. Wang, C.; Wang, Y.; Xiao, W.; Chen, X.; Li, R.; Shen, Z.; Lu, F. Carboxylated superparamagnetic Fe_3O_4 nanoparticles modified with 3-amino propanol and their application in magnetic resonance tumor imaging. *BMC Cancer* **2023**, *23*, 54. [CrossRef]
28. Villa, S.; Riani, P.; Locardi, F.; Canepa, F. Functionalization of Fe_3O_4 NPs by Silanization: Use of Amine (APTES) and Thiol (MPTMS) Silanes and Their Physical Characterization. *Materials* **2016**, *9*, 826. [CrossRef] [PubMed]
29. Pakravanan, K.; Bazzurro, V.; Salerno, M.; Diaspro, A. Uptake of gold nanoparticles in HeLa cells observed by confocal microscopy shows dependency on particle size and shape. *Eur. Biophys. J.* **2025**, 1–12, *ahead of print*. [CrossRef]
30. Mei, C.; Yang, Y.; Dong, P.; Song, L.; Zhou, Y.; Xu, Y.; Yu, C. Deficiency of PKClambda/iota alleviates the liver pathologic impairment of *Schistosoma japonicum* infection by thwarting Th2 response. *Parasit. Vectors* **2022**, *15*, 154. [CrossRef]
31. *GB19489-2008*; Laboratories—General Requirements for Biosafety. The State Administration for Quality Supervision, Inspection and Quarantine of the People's Republic of China and the China National Standardization Administration Committee: Beijing, China, 2008.
32. Song, L.J.; Luo, H.; Fan, W.H.; Wang, G.P.; Yin, X.R.; Shen, S.; Wang, J.; Jin, Y.; Zhang, W.; Gao, H.; et al. Oxadiazole-2-oxides may have other functional targets, in addition to SjTGR, through which they cause mortality in *Schistosoma japonicum*. *Parasit. Vectors* **2016**, *9*, 26. [CrossRef]
33. Gong, W.; Huang, F.; Sun, L.; Yu, A.; Zhang, X.; Xu, Y.; Shen, Y.; Cao, J. Toll-like receptor-2 regulates macrophage polarization induced by excretory-secretory antigens from *Schistosoma japonicum* eggs and promotes liver pathology in murine schistosomiasis. *PLoS Negl. Trop. Dis.* **2018**, *12*, e0007000. [CrossRef]
34. De Marco Verissimo, C.; Potriquet, J.; You, H.; McManus, D.P.; Mulvenna, J.; Jones, M.K. Qualitative and quantitative proteomic analyses of *Schistosoma japonicum* eggs and egg-derived secretory-excretory proteins. *Parasit. Vectors* **2019**, *12*, 173. [CrossRef]
35. Dalton, J.P.; Day, S.R.; Drew, A.C.; Brindley, P.J. A method for the isolation of schistosome eggs and miracidia free of contaminating host tissues. *Parasitology* **1997**, *115*, 29–32. [CrossRef]
36. Yoshimoto, S.; Taguchi, M.; Sumi, S.; Oka, K.; Okamura, K. Establishment of a novel protocol for formalin-fixed paraffin-embedded organoids and spheroids. *Biol. Open* **2023**, *12*, 059882. [CrossRef] [PubMed]
37. Mpelane, S.; Mketo, N.; Bingwa, N.; Nomngongo, P.N. Synthesis of mesoporous iron oxide nanoparticles for adsorptive removal of levofloxacin from aqueous solutions: Kinetics, isotherms, thermodynamics and mechanism. *Alex. Eng. J.* **2022**, *61*, 8457–8468. [CrossRef]
38. Kang, D.; Lee, M.; Lee, S.J.; Kim, J.-H.; Ryu, G.H. Enhanced Adhesion and Corrosion Resistance of Reduced Graphene Oxide Coated-Steel with Iron Oxide Nanoparticles. *Appl. Surf. Sci.* **2023**, *624*, 157121. [CrossRef]

39. Liu, Y.; Mo, H.; Shan, H.; Zhan, H.; Peng, S. Effect of Fe(II) and Fe(III) doping levels on the structural and binding mechanism of graphene oxide chitosan: Spectral analysis and density function theory calculation. *Int. J. Biol. Macromol.* **2025**, *317*, 144635. [CrossRef]
40. You, Y.; Chen, X.; Huo, L.; Chen, L.; Chen, G.; Gu, M.; Yi, C.; Wang, J.; Hu, W. An improved medium for in vitro studies of female reproduction and oviposition in *Schistosoma japonicum*. *Parasit. Vectors* **2024**, *17*, 116. [CrossRef] [PubMed]
41. Wilson, M.S.; Mentink-Kane, M.M.; Pesce, J.T.; Ramalingam, T.R.; Thompson, R.; Wynn, T.A. Immunopathology of schistosomiasis. *Immunol. Cell Biol.* **2007**, *85*, 148–154. [CrossRef]
42. Zhong, H.; Gui, X.; Hou, L.; Lv, R.; Jin, Y. From Inflammation to Fibrosis: Novel Insights into the Roles of High Mobility Group Protein Box 1 in Schistosome-Induced Liver Damage. *Pathogens* **2022**, *11*, 289. [CrossRef]
43. Dewalick, S.; Bexkens, M.L.; van Balkom, B.W.; Wu, Y.P.; Smit, C.H.; Hokke, C.H.; de Groot, P.G.; Heck, A.J.; Tielens, A.G.; van Hellemond, J.J. The proteome of the insoluble *Schistosoma mansoni* eggshell skeleton. *Int. J. Parasitol.* **2011**, *41*, 523–532. [CrossRef]
44. Llanwarne, F.; Helmby, H. Granuloma formation and tissue pathology in *Schistosoma japonicum* versus *Schistosoma mansoni* infections. *Parasite Immunol.* **2021**, *43*, e12778. [CrossRef]
45. Hams, E.; Aviello, G.; Fallon, P.G. The schistosoma granuloma: Friend or foe? *Front. Immunol.* **2013**, *4*, 89. [CrossRef]
46. Wu, W.; Wang, W.; Huang, Y. New insight into praziquantel against various developmental stages of schistosomes. *Parasitol. Res.* **2011**, *109*, 1501–1507. [CrossRef]
47. Reddy, L.H.; Arias, J.L.; Nicolas, J.; Couvreur, P. Magnetic nanoparticles: Design and characterization, toxicity and biocompatibility, pharmaceutical and biomedical applications. *Chem. Rev.* **2012**, *112*, 5818–5878. [CrossRef] [PubMed]
48. Medintz, I.L.; Mattoussi, H.; Clapp, A.R. Potential clinical applications of quantum dots. *Int. J. Nanomed.* **2008**, *3*, 151–167. [CrossRef] [PubMed]
49. Candido, R.R.F.; Morassutti, A.L.; Graeff-Teixeira, C.; St. Pierre, T.G.; Jones, M.K. Exploring Structural and Physical Properties of Schistosome Eggs: Potential Pathways for Novel Diagnostics? *Adv. Parasitol.* **2018**, *100*, 209–237. [CrossRef]
50. Liu, C.; Jiang, X.; Gan, Y.; Yu, M. Engineering nanoparticles to overcome the mucus barrier for drug delivery: Design, evaluation and state-of-the-art. *Med. Drug Discov.* **2021**, *12*, 100110. [CrossRef]
51. Zheng, G.; Zhang, B.; Yu, H.; Song, Z.; Xu, X.; Zheng, Z.; Zhao, K.; Zhao, J.; Zhao, Y. Therapeutic applications and potential biological barriers of nano-delivery systems in common gastrointestinal disorders: A comprehensive review. *Adv. Compos. Hybrid. Mater.* **2025**, *8*, 227. [CrossRef]
52. Mitchell, M.J.; Billingsley, M.M.; Haley, R.M.; Wechsler, M.E.; Peppas, N.A.; Langer, R. Engineering precision nanoparticles for drug delivery. *Nat. Rev. Drug Discov.* **2021**, *20*, 101–124. [CrossRef] [PubMed]
53. Van Hellemond, J.J.; Retra, K.; Brouwers, J.F.; van Balkom, B.W.; Yazdanbakhsh, M.; Shoemaker, C.B.; Tielens, A.G. Functions of the tegument of schistosomes: Clues from the proteome and lipidome. *Int. J. Parasitol.* **2006**, *36*, 691–699. [CrossRef] [PubMed]
54. Wilson, R.A.; Barnes, P.E. The tegument of *Schistosoma mansoni*: Observations on the formation, structure and composition of cytoplasmic inclusions in relation to tegument function. *Parasitology* **1974**, *68*, 239–258. [CrossRef] [PubMed]

Disclaimer/Publisher's Note: The statements, opinions and data contained in all publications are solely those of the individual author(s) and contributor(s) and not of MDPI and/or the editor(s). MDPI and/or the editor(s) disclaim responsibility for any injury to people or property resulting from any ideas, methods, instructions or products referred to in the content.